



HAL
open science

Classifying IGR J18007-4146 as an intermediate polar using XMM and NuSTAR

Benjamin M. Coughenour, John A. Tomsick, Aarran W. Shaw, Koji Mukai,
Maïca Clavel, Jeremy Hare, Roman Krivonos, Francesca M. Fornasini

► **To cite this version:**

Benjamin M. Coughenour, John A. Tomsick, Aarran W. Shaw, Koji Mukai, Maïca Clavel, et al..
Classifying IGR J18007-4146 as an intermediate polar using XMM and NuSTAR. *Monthly Notices of
the Royal Astronomical Society*, 2022, 511, pp.4582-4589. 10.1093/mnras/stac263 . insu-03705354

HAL Id: insu-03705354

<https://insu.hal.science/insu-03705354>

Submitted on 24 Mar 2023

HAL is a multi-disciplinary open access archive for the deposit and dissemination of scientific research documents, whether they are published or not. The documents may come from teaching and research institutions in France or abroad, or from public or private research centers.

L'archive ouverte pluridisciplinaire **HAL**, est destinée au dépôt et à la diffusion de documents scientifiques de niveau recherche, publiés ou non, émanant des établissements d'enseignement et de recherche français ou étrangers, des laboratoires publics ou privés.

Classifying IGR J18007–4146 as an intermediate polar using *XMM* and *NuSTAR*

Benjamin M. Coughenour¹,^{1★} John A. Tomsick,¹ Aarran W. Shaw^{1,2},² Koji Mukai,^{3,4} Maïca Clavel,⁵ Jeremy Hare,^{6†} Roman Krivonos⁷ and Francesca M. Fornasini^{1,8}

¹Space Sciences Laboratory, 7 Gauss Way, University of California, Berkeley, CA 94720-7450, USA

²Department of Physics, University of Nevada, Reno, NV 89557, USA

³CRESST and X-ray Astrophysics Laboratory, NASA Goddard Space Flight Center, Greenbelt, MD 20771, USA

⁴Department of Physics, University of Maryland, Baltimore County, 1000 Hilltop Circle, Baltimore, MD 21250, USA

⁵Université Grenoble Alpes, CNRS, IPAG, F-38000 Grenoble, France

⁶NASA Goddard Space Flight Center, Greenbelt, MD 20771, USA

⁷Space Research Institute, Russian Academy of Sciences, Profsoyuznaya 84/32, 117997 Moscow, Russia

⁸Department of Physics and Astronomy, Stonehill College, 320 Washington Street, Easton, MA 02357, USA

Accepted 2022 January 26. Received 2022 January 25; in original form 2021 November 22

ABSTRACT

Many new and unidentified Galactic sources have recently been revealed by ongoing hard X-ray surveys. A significant fraction of these have been shown to be the type of accreting white dwarfs known as cataclysmic variables (CVs). Follow-up observations are often required to categorize and classify these sources, and may also identify potentially unique or interesting cases. One such case is IGR J18007–4146, which is likely a CV based on follow-up *Chandra* observations and constraints from optical/IR catalogues. Utilizing simultaneous *XMM–Newton* and *NuSTAR* observations, as well as the available optical/IR data, we confirm the nature of IGR J18007–4146 as an intermediate polar type CV. Timing analysis of the *XMM* data reveals a periodic signal at 424.4 ± 0.7 s that we interpret as the spin period of the white dwarf. Modelling the 0.3–78 keV spectrum, we use a thermal bremsstrahlung continuum but require intrinsic absorption as well as a soft component and strong Fe lines between 6 and 7 keV. We model the soft component using a single-temperature blackbody with $kT = 73_{-6}^{+8}$ eV. From the X-ray spectrum, we are able to measure the mass of the white dwarf to be $1.06_{-0.10}^{+0.19} M_{\odot}$, which means IGR J18007–4146 is more massive than the average for magnetic CVs.

Key words: accretion, accretion discs – stars: individual (IGR J18007–4146) – novae, cataclysmic variables – white dwarfs – X-rays: binaries.

1 INTRODUCTION

Since its launch in 2002, the *International Gamma-Ray Astrophysics Laboratory* (*INTEGRAL*) has covered the entire sky with increasing depth above 20 keV, detecting over 1000 distinct hard X-ray sources. While most of these sources were previously known, having been detected with soft X-ray instruments, *INTEGRAL*'s wide field of view and broad high-energy coverage has led to the discovery of hundreds of new hard X-ray sources, referred to as *INTEGRAL* Gamma-ray (IGR) sources. While most of these are active galactic nuclei, many are Galactic accreting sources such as cataclysmic variables (CVs) or neutron star and black hole X-ray binaries. Still, many sources (>200) remain unclassified (Bird et al. 2016; Krivonos et al. 2017, 2022).

A clear strategy to classify unknown sources is to use follow-up observations, particularly in the soft X-ray band where these sources may be localized to better accuracy than *INTEGRAL*'s \sim arcminute angular resolution. In order to study and classify Galactic IGR

sources, Tomsick et al. (2020) used *Chandra* follow-up observations of unclassified IGR sources from the Bird et al. (2016) catalogue within 15° of the Galactic plane. Of the 15 selected unclassified targets, 10 likely (in some cases certain) *Chandra* counterparts were detected, among which IGR J18007–4146, IGR J15038–6021, and IGR J17508–3219 are most likely Galactic sources based on *Gaia* parallax distances. Of these, the former two are likely CVs or intermediate polars (IPs), with the possibility of high-mass donor stars being ruled out by their optical/IR counterparts (Tomsick et al. 2020). As was the case with other CVs discovered in the high-energy band of *INTEGRAL*, such as the high-mass magnetic CV (mCV) IGR J14091–6108 (Tomsick et al. 2016), these candidate CVs are interesting sources worthy of additional study. In this paper, we focus our investigation on the source IGR J18007–4146.

In mCVs, the accretion disc is truncated well above the white dwarf (WD) surface, if one forms at all (truncated discs are typical of IPs but not of polars). These systems produce hard X-rays due to accretion along the magnetic field lines of the WD. When this accretion column slows from its free-fall velocity very near the WD surface, the resultant shock heats the material to extraordinary temperatures, and as the accreted material cools, it does so via bremsstrahlung radiation, producing hard X-rays (see Patterson 1994; Warner 2003, for a review

* E-mail: coughenour@berkeley.edu

† NASA Postdoctoral Program Fellow

Table 1. Observations of IGR J18007–4146.

Observatory	ObsID	Instrument	Start time (UT)	End time (UT)	Exposure time (ks)
<i>XMM</i>	0870790201	pn	2020 Oct 3, 15.24 h	2020 Oct 3, 23.20 h	23.2
"	"	MOS1	2020 Oct 3, 15.79 h	2020 Oct 3, 23.29 h	25.1
"	"	MOS2	2020 Oct 3, 16.20 h	2020 Oct 3, 23.29 h	23.7
<i>NuSTAR</i>	30601017002	FPMA	2020 Oct 3, 9.44 h	2020 Oct 4, 6.02 h	39.9
"	"	FPMB	"	"	39.6

of CVs). In particular, when these sources are observed in the hard X-ray band with instruments like *NuSTAR*, measurements of the shock temperature (a cut-off in the high-energy spectrum) provide a direct estimate of the WD mass (Hailey et al. 2016; Suleimanov et al. 2016; Shaw et al. 2018, 2020; Suleimanov, Poutanen & Werner 2018). Since a higher bremsstrahlung temperature is a natural consequence of a more massive WD, IPs detected in the *INTEGRAL* band may be biased towards higher mass WDs.

To confirm the CV nature of IGR J18007–4146 (hereafter IGR J18007) and closely investigate its properties, we carried out joint *XMM–Newton* and *NuSTAR* observations of the source and investigated its spectral and timing properties. In Section 2, we describe these observations and the data reduction. In Section 3, we describe our timing analysis and search for periodicity in the source light curve (3.1) as well as our modelling of the source energy spectra (3.2). Finally, we discuss these results and their implications in Section 4.

2 OBSERVATIONS AND DATA REDUCTION

Observations of IGR J18007 were carried out simultaneously with the *X-ray Multi-Mirror Mission (XMM–Newton)* and the *Nuclear Spectroscopic Telescope Array (NuSTAR)* beginning on 2020 October 3, with the *NuSTAR* observation lasting until 2020 October 4. In the case of *XMM–Newton* (Jansen et al. 2001), the duration of the observation was 37.5 ks. The longer *NuSTAR* (Harrison et al. 2013) observation produced ~ 40 ks of exposure in each Focal Plane Module (known as FPMA and FPMB) after dead-time corrections and Earth occultations. These observation details are summarized in Table 1.

2.1 XMM

We reduced the EPIC/pn (Strüder et al. 2001) and EPIC/MOS (Turner et al. 2001) data with the XMM Science Analysis Software v18.0.0 using the standard analysis procedures provided online.¹ All three detectors (pn, MOS1, and MOS2) were operated in Full Window mode with the medium optical-blocking filter. We used the SAS routine `epatplot` to determine that no significant photon pile-up is present in pn, MOS1, or MOS2. For the pn, we filtered the photon event lists requiring the FLAG parameter to be zero and the PATTERN parameter to be less than or equal to 4. For MOS, we used the filtering expression, ‘#XMMEA_EM && (PATTERN<=12).’

The pn and MOS images show a single bright source at the *Chandra* position of IGR J18007. We extracted a 0.3–12 keV pn light curve using a circular source region centred on IGR J18007 with a radius of 640 pixels (32 arcsec) along with a background light curve. We specified a time resolution of 100 s, and the background-subtracted pn light curve is shown in the top panel of Fig. 1. Although the source does not show any dramatic variability, a low-level of variability is apparent.

¹See <https://www.cosmos.esa.int/web/xmm-newton/sas-threads>

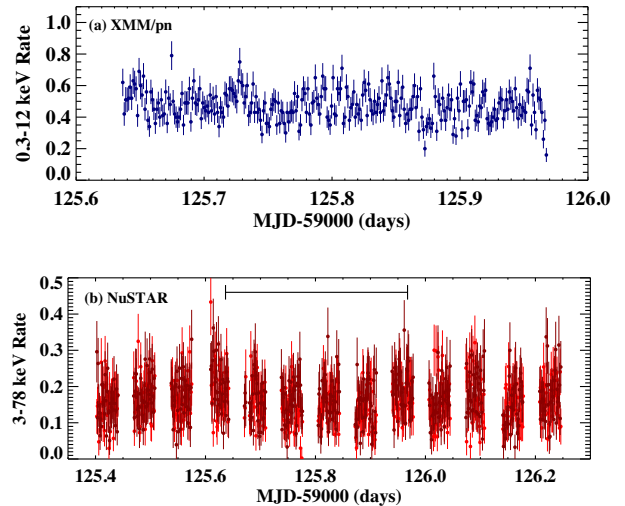


Figure 1. Light curves shown for (a) *XMM* and (b) *NuSTAR*, with FPMA/B shown in light/dark red, respectively. Note the different x-axis scale between the two light curves; the shorter duration of the *XMM* observation is illustrated at the top of the *NuSTAR* light curve with a horizontal bar.

We also extracted a 10–12 keV pn light curve with 100 s time bins including photons from the entire field of view. This is done to determine if there are background particle flares, and we find that this observation includes a few flares. We created a good time interval (gti) filter to include only the times when the count rate in the 10–12 keV pn light curve is less than 0.5 c s^{-1} . After filtering out the background flares, we extracted source and background energy spectra. We used the same gti filter for pn, MOS1, and MOS2 in order to maintain near-simultaneity between the instruments. After using `evselect` to extract source and background spectra, we used `backscale` to set the background scaling parameter, which accounts for the size of the extraction regions and any bad pixels in the regions. In addition, we used `rmfgen` and `arfgen` to produce the response matrices. We binned the spectra to require a signal-to-noise ratio of 5 in each bin (except the highest energy bin). The fitting of the spectra is described in Section 3.2.

2.2 NuSTAR

NuSTAR ObsID 30601017002 was reduced using NUSTARDAS v2.0.0 and CALDB 20210427. Standard data products were produced with `nupipeline`, including 3–78 keV images for both FPMA and FPMB. For the timing analysis, barycentre-corrected event files were created using `nuproducts`. Using these images, circular regions of 60 and 90 arcsec in radius were chosen for the source and background regions. IGR J18007 was clearly visible, and the background region was positioned to be on the same detector chip as the source. The 3–78 keV spectra were then extracted using `nuproducts` for both FPMA and FPMB, and these spectra were

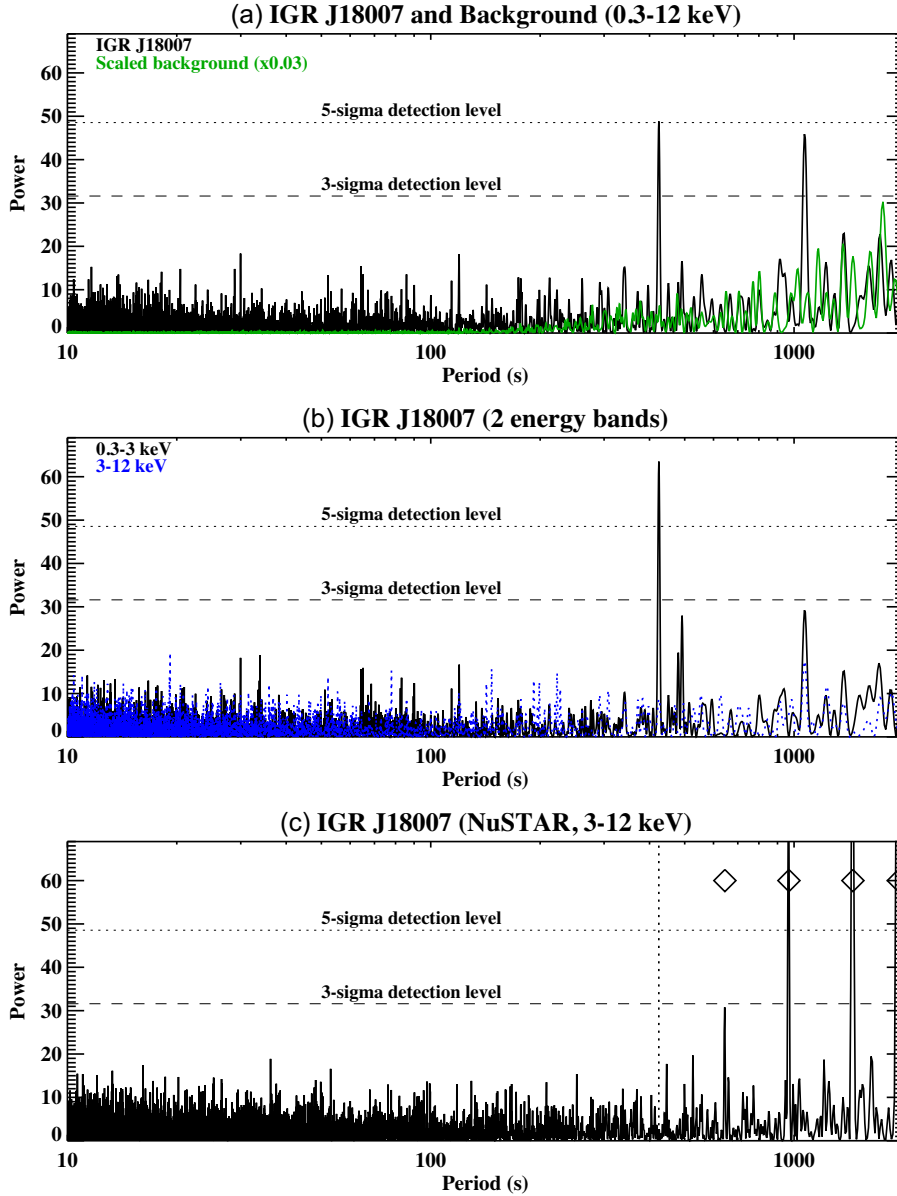


Figure 2. (a) The results of a Z_1^2 (Rayleigh) test periodicity search using all 0.3–12 keV photons in the circular source (J18007) regions for the pn, MOS1, and MOS2 instruments onboard *XMM*. The green curve shows the scaled background periodogram. (b) Periodograms for J18007 in the 0.3–3 and 3–12 keV energy bands, showing the high significance of the 424.4 ± 0.7 s period in the soft band. (c) Periodogram for the 3–12 keV summed FPMA/B light curve from *NuSTAR*, which does not detect the 424.4 s period signal seen with *XMM* (vertical dotted line). The open diamonds denote harmonics of the *NuSTAR* orbital period.

then each binned using `grppha` to require a signal-to-noise ratio of 5 in each bin (except the highest energy bin), as was done for the 0.3–12 keV *XMM-Newton* spectra (see Section 2.1). The background-subtracted light curves for *NuSTAR* FPMA and FPMB are shown together in the bottom panel of Fig. 1.

3 RESULTS

3.1 X-ray timing

For the *XMM/EPIC* instruments (pn, MOS1, and MOS2), we made event lists including the 0.3–12 keV photons in the same circular source regions used for the spectral analysis. We corrected the timestamp for each event to the time at the Solar system barycentre using the SAS routine `barycen`. Given that the results of Tomsick

et al. (2020) strongly suggest that IGR J18007 is an IP (this is also supported by our spectral analysis, see Section 3.2), we carried out a search for a periodic signal, which is often seen at the WD spin period for IPs. We used the Z_1^2 test (Buccheri et al. 1983) to search for a periodic signal in 20 000 evenly spaced frequency bins between 5×10^{-4} and 0.1 Hz, corresponding to periods between 10 and 2000 s. The range of periods searched is based on typical WD spin periods in IPs (de Martino et al. 2020), and the number of bins is set to oversample the number of independent frequencies by a factor of eight. Although the specific oversampling number is not critical, some oversampling is necessary to ensure that the peaks seen are not biased by the exact value of the starting frequency.

The results of the periodicity search are shown in Fig. 2(a). The false alarm probability (FAP) for this test is given by $N_{\text{trials}} e^{-S/2}$,

where S is the peak signal power and N_{trials} is the number of frequencies searched. In this case, the 3σ detection level, corresponding to $\text{FAP} = 2.7 \times 10^{-3}$, is at $S = 31.6$. There are two peaks in the periodogram above the 3σ level. The strongest (at $S = 48.8$) is at 424.4 ± 0.7 s, and a slightly weaker ($S = 46.2$) signal is at 1069.5 ± 3.0 s. The 1σ uncertainties on the periods are found by determining where the signal drops to a signal power of $S-1$. The FAPs for the 424.4 and 1069.5 s signals are 5.1×10^{-7} (5σ) and 1.9×10^{-6} (4.75σ), respectively.

We also performed a periodicity search with the *NuSTAR* data using the Z_1^2 test and the same 20000 trial periods used for *XMM*, which, as for *XMM*, puts the 3σ significance threshold at $S = 31.6$. We used event lists that include photons detected by FPMA and FPMB in three energy bands (3–6, 3–12, and 3–78 keV). All the peaks in the periodogram that exceed $S = 31.6$ are harmonics of the *NuSTAR* orbital period. Peaks are seen at 968, 1452, and 1936 s, and they are expected due to Earth occultations. There are no significant peaks in the *NuSTAR* periodograms at either of the *XMM* periods. At 424.4 and 1069.5 s, the 3–12 keV *NuSTAR* periodogram has values of $S = 1.9$ and $S = 3.7$, respectively, and this periodogram is given in Fig. 2(c).

Given the lack of detection of the *XMM* periods in the *NuSTAR* periodograms, we made additional *XMM* periodograms in the 0.3–3 and 3–12 keV energy bands to check on the energy dependence of the signals. Fig. 2(b) shows that the 424.4 s signal has $S = 63.5$ at 0.3–3 keV, which, even after accounting for the extra trials, corresponds to a significance above 6σ . In comparison, the 3–12 keV periodogram has a value of $S = 8.8$ at 424.4 s. The fact that the 424.4 s signal is not detected in the 3–12 keV band but is strong at 0.3–3 keV indicates that it has an extremely soft spectrum, which is consistent with the fact that it is not seen by *NuSTAR*. The 1069.5 s signal is not detected at the 3σ level in either energy band individually, but the ratio of the strength of the 0.3–3 keV peak to the 3–12 keV peak is much smaller than for 424.4 s, indicating that if it is a real signal, it has a much harder spectrum. While the softness of the 424.4 s signal provides a plausible explanation for why we do not see it in the *NuSTAR* periodogram, it is somewhat surprising that we do not see any evidence for a peak at 1069.5 s with *NuSTAR*. Thus, we focus on the 424.4 s signal in the rest of this section.

The 424.4 s signal is seen in each instrument individually, increasing our confidence that it is a real signal from IGR J18007. However, we carried out an additional check because there is variability in the background, and the Z_1^2 test uses a photon list which is not background subtracted. In addition, we did not filter the photon list for times of high background because putting gaps in the data can also cause spurious signals. Thus, we carried out an identical analysis to the Z_1^2 test that led to the detection of the 424.4 s signal in IGR J18007, but we used a photon list from the next brightest source in the field. The comparison source is much fainter than IGR J18007, making it a good test of whether the background can induce a spurious signal. The result for the comparison source is that the power of the strongest peak is $S = 16.8$, which is consistent with a non-detection. Furthermore, at 424.4 s, the power is $S = 2.4$, confirming that the background variability does not induce a peak at the IGR J18007 detection period. Another demonstration that the background is not inducing the 424.4 s is that we made a background periodogram taken from large regions of the pn, MOS1, and MOS2 fields, and this is shown in Fig. 2(a).

We carried out an epoch folding analysis with the 0.3–12 keV *XMM* pn and MOS light curves. This provides another check on the detection of the period since we perform the folding with a background-subtracted light curve. Folding at a range of trial periods

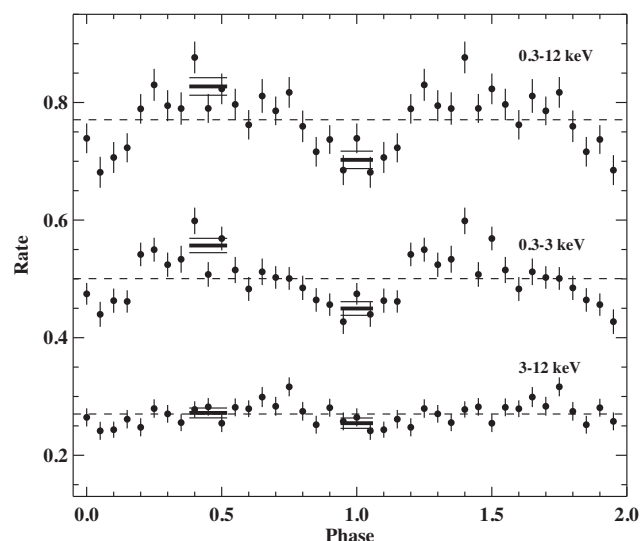


Figure 3. *XMM* light curves folded on a period of 424.4 s. The count rate plotted is the sum of the pn, MOS1, and MOS2 rates, in three different energy bands. On top is the full count rate (0.3–12 keV), which is the sum of the soft (0.3–3 keV, middle) and hard (3–12 keV, bottom) count rates. The thick solid horizontal lines show the average of the three points at the minimum and maximum phases, as defined by the phase of the full count rate. The thin solid horizontal lines show the 1σ uncertainties on the averages. Two cycles of the period are shown for clarity.

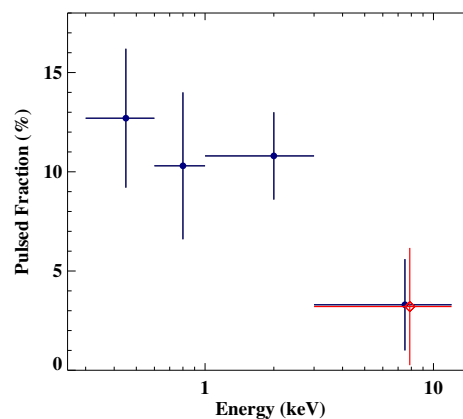


Figure 4. The pulsed fraction versus energy for *XMM* (filled circles) and *NuSTAR* (red diamond). The *XMM* points include the pn, MOS1, and MOS2 data, while *NuSTAR* shows the combined FPMA/B. The pulsed fraction is determined from the folded light curves, and is defined as maximum minus minimum divided by maximum plus minimum. The uncertainties shown are at the 1σ confidence level.

yields peaks for pn and MOS consistent with the 424.4 s signal. We combined the pn, MOS1, and MOS2 light curves after trimming them to have the same start and stop times (which we also did for the Z_1^2 test described above). Fig. 3 shows the result of folding specifically on the 424.4 s period, and a significant modulation can be seen in the 0.3–3 and 0.3–12 keV energy bands, but less so in the 3–12 keV band. The maxima and minima and their uncertainties are marked, and we calculate the pulsed fraction as maximum minus minimum divided by maximum plus minimum. We find a 0.3–12 keV pulsed fraction of $8.2 \text{ per cent} \pm 1.4 \text{ per cent}$. We repeated the analysis in four energy bands using the maximum and minimum phase ranges from the 0.3–12 keV analysis, and Fig. 4 summarizes these results. There

is no evidence for a difference in amplitude between 0.3 and 3 keV with the average being 11 per cent, but the 3–12 keV amplitude is significantly lower with a value of 3.2 per cent \pm 2.3 per cent, which is consistent with a non-detection.

We also performed a folding analysis of the *NuSTAR* light curves specifically at the 424.4 s period detected in the *XMM* data. We first shifted the *NuSTAR* light curve by matching the start time to the phase zero epoch found with *XMM*. Then, we calculated the maximum and minimum values in the folded light curve using the maximum and minimum phase ranges from the 0.3–12 keV *XMM* analysis to determine the pulsed fraction for the 3–12 keV *NuSTAR* band. This analysis was performed separately for FPMA and FPMB. Although no statistically significant detection was obtained, the measurements are consistent with *XMM*. In the 3–12 keV band, we find 3.2 per cent \pm 3.0 per cent, and this point is shown along with the *XMM* values in Fig. 4.

3.2 X-ray spectrum

For spectral analysis, we used the XSPEC package v12.11.1 (Arnaud 1996) and performed the fitting with χ^2 minimization. Spectra from each of the five separate detectors, EPIC/pn and EPIC/MOS[1/2] from *XMM-Newton*, as well as FPM[A/B] from *NuSTAR*, were fit together using the XSPEC model CONSTANT, with the factor for the EPIC/pn spectrum set fixed to 1.0 and all others allowed to vary. This is in order to account for any calibration differences between the different instruments. Interstellar absorption was taken into account using the model TBABS, with Wilms et al. (2001) abundances. Errors quoted in our spectral analysis represent the 90 per cent confidence level.

Initial fits using an absorbed power law with a high-energy cut-off (CUTOFFPL in XSPEC) showed that the source spectrum is very hard up to \sim 30 keV, with a photon index of 0.93 ± 0.03 . This value is consistent with the reported results of Tomsick et al. (2020) using *Chandra* and *INTEGRAL* data, and suggests that IGR J18007 is either a CV or HMXB. Residuals in the 6–7 keV range and below 1 keV imply the presence of Fe line emission and a soft thermal component. Indeed, including a low-temperature (\sim 0.1 keV) blackbody (with BBODYRAD) as well as a broad Gaussian Fe line at 6.5 keV dramatically improved the fit to $\chi^2 = 929$ with 845 degrees of freedom (dof).

Considering that IGR J18007 is likely an IP, we continue our spectral analysis using a more physical model. Bremsstrahlung emission is expected to produce the majority of the continuum source emission, as is generally the case for mCVs (Mukai 2017), and we chose the model BREMSS to represent the broad continuum, modified by reflection off of neutral material (in this case, the WD surface) using REFLECT in XSPEC (Magdziarz & Zdziarski 1995). We replaced the single, broad emission line measured at 6.5 ± 0.4 keV from our initial fits with three individual Gaussians fixed at 6.40, 6.70, and 6.97 keV to represent the reflected neutral Fe K α line alongside the Fe XXV and Fe XXVI ionization states, respectively. At first we tied the Gaussian σ values together, to prevent a single line from broadening to cover the others, but found their widths to be poorly constrained and unrealistically high (with $\sigma \sim 200$ eV). To fix this we froze the width of each line to be $\sigma = 50$ eV to better represent the expected narrow emission lines, and we found all three lines to be significantly detected when using the narrow Gaussians. Each line was inconsistent with a zero normalization at $>4\sigma$ as calculated using `steppar` in XSPEC.

At first, this more physical model provided a poor fit to the data, with the model deviating significantly from the spectra below

\sim 3 keV. An additional feature in the residuals is a noticeable bump at \sim 16 keV, though this has no clear physical interpretation, and we found that the presence of an additional Gaussian at 16 keV is not highly significant. As for the low-energy residuals, we included intrinsic absorption using a partial-covering absorber with the model PCFABS. This immediately made a dramatic improvement to the fit, with a reduction in the fit statistic $\Delta\chi^2 = 144$ for two fewer dof. Some intrinsic partial covering absorption is expected in mCVs because the cooling post-shock accretion material near the WD surface is beneath the rest of the accelerating accretion flow, and may be covered or absorbed depending on the accretion geometry and line of sight (Norton & Watson 1989). The additional absorption model component is therefore both physically and statistically motivated, and provides more evidence supporting the IP nature of IGR J18007. We also tested whether the partial covering absorption is able to fit the low-energy spectra without the need for a soft component, but we found that both are required to produce even a reasonable fit to the spectra. This reflected bremsstrahlung continuum model, with partial covering absorption, three distinct Fe lines, and a soft component, provided an excellent fit to the data, with $\chi^2/\text{dof} = 840/842$, and we measure a bremsstrahlung plasma temperature of $24.2_{-2.0}^{+7.3}$ keV.

As a final test of the soft component, we also fit the spectra using the cooling flow model MKCFLOW (Mushotzky & Szymkowiak 1988), which includes atomic emission lines as well as an optically thin thermal continuum. Since MKCFLOW reproduces the 6.70 and 6.97 keV Fe lines, we removed the two higher energy Gaussians but kept the 6.40 keV line produced by reflection. A series of emission lines below 1 keV could conceivably reproduce the soft excess without the need for a blackbody, and so by modelling the spectra with MKCFLOW we tested the physicality of the soft blackbody component. We found that the blackbody still significantly improves our fits, and is required to satisfactorily fit the source spectrum alongside the partial covering absorption. Furthermore, we found that the blackbody temperature when using the cooling flow model does not significantly change from our results with a bremsstrahlung continuum, with both measurements consistent with $kT = 71$ eV at the 90 per cent confidence level. The MKCFLOW model also gives a measure of the maximum plasma temperature, and we find $T_{\text{max}} = 67_{-20}^{+13}$ keV, which is consistent with the hard-coded upper limit of the model at 79.9 keV.

3.2.1 Measuring the WD mass

In order to measure the WD mass, we replace the bremsstrahlung continuum emission with an updated version of the IP mass model of Suleimanov, Revnivtsev & Ritter (2005), referred to as the post-shock region or ‘PSR’ model (IPOLAR in XSPEC) and described in Suleimanov et al. (2016, 2019). As with our bremsstrahlung continuum model, we continue to use reflection, partial covering absorption, a blackbody soft component, and three Gaussian emission lines with the PSR model continuum. Previous versions of the PSR model calculated the shock temperature using the free-fall velocity of incoming material, which is a reasonable approximation for many CVs. However, by not taking into account the finite magnetospheric radius at which the accretion disc is truncated, the WD mass may be systematically underestimated (Suleimanov et al. 2016; Shaw et al. 2020). This updated PSR model takes into account a limited fall height in order to avoid such a bias. Following the method of Suleimanov et al. (2019) and Shaw et al. (2020), we set the magnetospheric radius equal to the co-rotation radius between the

WD and inner accretion disc:

$$R_m \simeq R_{\text{co}} = \left(\frac{GM_{\text{WD}} P_{\text{spin}}^2}{4\pi^2} \right)^{1/3} \quad (1)$$

The assumption that the co-rotation radius and magnetospheric radius are equal is acceptable if the IP has been persistently accreting, allowing the WD to reach spin equilibrium with material in the disc. Though we measure two periodic signals in the *XMM* data, we interpret the stronger and softer signal at 424.4 s to be the WD spin period, and we set the fall height parameter of the PSR model to vary according to the WD mass and spin period, using the equation above alongside the mass–radius relationship for WDs as calculated by Nauenberg (1972). The only free parameters of our IP model then are the WD mass and normalization.

As was the case for the bremsstrahlung continuum model, we obtain an excellent statistical fit using the PSR model as described, with $\chi^2/\text{dof} = 844/842$. Our best-fitting results using the PSR IP mass model are summarized in Table 2, and a plot of the unfolded spectrum and normalized residuals is shown in Fig. 5. For the WD mass, we measure $1.06_{-0.10}^{+0.19} M_{\odot}$, which gives a corresponding fall height of $17.4 R_{\text{WD}} = 8.7 \times 10^4$ km (assuming the Nauenberg 1972 mass–radius relationship). For the soft component, we measure a blackbody temperature of 73_{-6}^{+8} eV, which is consistent with our earlier results and is common for IPs and polars (de Martino et al. 2020).

4 DISCUSSION

IGR J18007 was chosen for follow-up investigation as a likely CV due to its hard X-ray spectrum and faint optical counterpart (Tomsick et al. 2020). Our results confirm this interpretation – with higher quality X-ray data, we still find a hard X-ray continuum, but also a strong Fe line complex between 6 and 7 keV, a distinct soft component (which is often seen in IPs), and intrinsic partial covering absorption. The three distinct Fe lines, with the weakest line at 6.97 keV detected at 4σ , provide evidence that the source is an accreting WD rather than a black hole or neutron star. We also detect periodic signals in the *XMM* data, which is expected of IPs but could also be explained by a slowly rotating neutron star in an HMXB or symbiotic X-ray binary. These possibilities are ruled out by optical/IR photometry. In Tomsick et al. (2020), the *Chandra* position of IGR J18007 is used to identify optical/IR counterparts in the VISTA and *Gaia* catalogues. Given the low extinction as measured by *Chandra* as well as the photometric IR colours, the authors estimated the companion temperature to be ~ 6500 K. This analysis is supported by the *StarHorse* data base (Anders et al. 2019), which reports an effective temperature of 6265 K. If the source were an HMXB or contained a late-type giant, then the companion would dominate the optical/IR flux and the temperature derived from photometry would represent the effective temperature of the companion. With this in mind, a temperature of ~ 6500 K is inconsistent with an HMXB or a symbiotic X-ray pulsar, and we conclude that IGR J18007 is indeed an IP accreting from a low-mass companion.

Gaia DR2 parallax data were instrumental in constraining the properties of the companion, but with an updated *Gaia* EDR3 geometric distance of $2.44_{-0.26}^{+0.28}$ kpc (Bailer-Jones et al. 2021; *Gaia* Collaboration 2021), we are able to better constrain the X-ray luminosity of IGR J18007 as well. Using this distance as well as the measured 0.3–100 keV flux of 1.08×10^{-11} erg cm $^{-2}$ s $^{-1}$ based off our PSR model, we calculate a luminosity of $7.7_{-1.6}^{+1.9} \times 10^{33}$ erg s $^{-1}$, which is typical of known IPs (de Martino et al. 2020). In the 17–60 keV *INTEGRAL* band, we measure a flux of 4.68×10^{-12} erg cm $^{-2}$ s $^{-1}$,

Table 2. Spectral results for PSR model.

CONSTANT*TBABS*PCFABS*(REFLECT*IPOLAR + BBODYRAD + 3 GAUSS)			
Model	Parameter	Units	Value
TBABS	N_{H}	10^{22} cm $^{-2}$	0.03 ± 0.02
	N_{H}	10^{22} cm $^{-2}$	11.7 ± 2.3
PCFABS	fraction	–	$0.63_{-0.12}^{+0.05}$
	$\Omega/2\pi$	–	1.0^a
REFLECT	A	–	$0.5_{-0.4}^{+0.7b}$
	$\cos i$	–	$0.65_{-0.41}^{+0.30c}$
IPOLAR	M_{WD}	M_{\odot}	$1.06_{-0.10}^{+0.19}$
	fall height	R_{WD}	17.4^d
	N_{PSR}	10^{-29}	$8.8_{-6.5}^{+6.6}$
BBODYRAD	kT	eV	73_{-6}^{+8}
	N	10^3	$3.9_{-2.6}^{+4.9}$
GAUSS ₁	E_1	keV	6.4^a
	σ_1	keV	0.05^a
	N_1	10^{-6} ph cm $^{-2}$ s $^{-1}$	11.9 ± 1.7
GAUSS ₂	E_2	keV	6.7^a
	σ_2	keV	0.05^a
	N_2	10^{-6} ph cm $^{-2}$ s $^{-1}$	6.7 ± 1.7
GAUSS ₃	E_3	keV	6.97^a
	σ_3	keV	0.05^a
	N_3	10^{-6} ph cm $^{-2}$ s $^{-1}$	3.8 ± 1.5
CONSTANT	C_{pn}	–	1.0^a
	C_{MOS1}	–	1.00 ± 0.03
	C_{MOS2}	–	0.99 ± 0.03
	C_{FPMA}	–	1.06 ± 0.04
	C_{FPMB}	–	1.15 ± 0.05
–	χ^2/dof	–	$844.4/842$

Note. Best-fitting results are shown for the PSR model of Suleimanov et al. (2016) and Suleimanov, Doroshenko & Werner (2019). This is included in the model description as ‘IPOLAR’ at the top of the table. As with the bremsstrahlung model, a blackbody soft component, intrinsic absorption, and three narrow Gaussian lines are included in the model. Errors represent 90 per cent confidence intervals.

^aFixed.

^bAbundance of elements heavier than He, including Fe, relative to solar values.

^cModel upper limit of 0.95 within 90 per cent confidence interval.

^dFixed to vary with WD mass and spin period.

and this is comparable to the 17-year average *INTEGRAL* flux of 7.9×10^{-12} erg cm $^{-2}$ s $^{-1}$ (Krivonos et al. 2022). Since CVs are naturally variable sources, this range of different flux measurements over time is to be expected.

In our timing analysis, we measure two periodic signals in the *XMM* data above the 3σ detection level, at 424.4 ± 0.7 s (5σ) and 1069.5 ± 3.0 s (4.75σ). Neither signal is present in the *NuSTAR* data, though the 424.4 s signal is very soft and is not detected above 3 keV in *XMM*. The 1069.5 s signal, however, is almost as significant above 3 keV as it is in the softer X-rays (but still below 3σ in either case). Spin periods in IPs are expected to have a soft spectrum (Mukai 2017), and a soft signal is consistent with partial covering absorption as well (Norton & Watson 1989). We therefore adopt the softer and more significant of the two detected signals (at 424.4 s) to be the spin period of the WD in IGR J18007. Folding at the 424.4 s period provides a clear pulse-profile (Fig. 3), and the pulsed fraction spectrum (Fig. 4) shows in detail that the spectrum is soft, and that the signal strength is consistent in both *XMM* and *NuSTAR* above

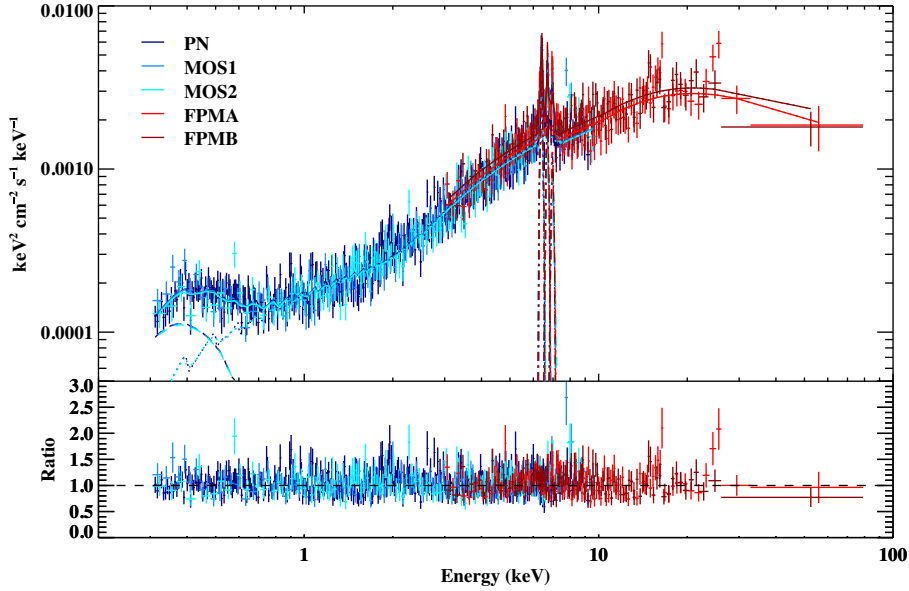


Figure 5. Unfolded *XMM* and *NuSTAR* energy spectrum fitted with the PSR IP mass model (see Table 2). The model consists of a low-temperature blackbody (dashed line), the broad PSR model (dotted line), and three narrow Gaussians between 6 and 7 keV (dash-dotted lines).

3 keV. A spin period of 424.4 s is well within the expected range among IPs (see e.g. de Martino et al. 2020), and the properties of the 424.4 s signal provide one more piece of evidence that IGR J18007 is an IP.

One curiosity of our spectral analysis worth discussing is the soft component which we model with a single-temperature blackbody. We measure a temperature of 73_{-6}^{+8} eV when using the PSR model. Soft components with temperatures less than 0.1 keV are often seen IPs (Mukai 2017; de Martino et al. 2020). Given the *Gaia* distance to IGR J18007, we estimate an emitting area with a radius of 15_{-10}^{+19} km, which is small with respect to the size of the WD. The physical interpretation of the soft component in the spectrum of an mCV is generally a matter of debate, particularly with respect to a partial absorber. In our case, this thermal emission may come from small hotspots on the WD surface close to its magnetic poles, heated by the nearby accretion column. Although typically modelled as a single-temperature blackbody, it is unlikely these hot regions would be isothermal (Beuermann, Burwitz & Reinsch 2012), and the interpretation of the soft component as a single-temperature blackbody is therefore physically unreliable. As an additional complication, it is unclear whether or not the soft component would then be subject to the same absorption as the hard X-rays from the accretion column, and in some instances the soft component may be an artefact of partial absorption on the continuum emission of the source. As described in Section 3.2, this is not the case for IGR J18007, and we are confident that a soft component is present and likely represents hotspots on the WD surface.

Using the PSR model of Suleimanov et al. (2016), we measure the WD mass to be $1.06_{-0.10}^{+0.19} M_{\odot}$. This mass measurement is slightly dependent on the fall height of material from the inner accretion disc, as opposed to IP models that rely on the assumption that in-falling material has reached its free-fall velocity. We take this into account by assuming the detected 424.4 s signal represents the WD spin period, and we set the WD magnetospheric radius to be equal to the co-rotation radius of the inner accretion disc. This provides the fall-height of accreted material, relative to the mass

of the WD as described in Section 3.2. Equating the magnetospheric and co-rotation radius is acceptable for persistently accreting IPs such as IGR J18007, where the WD and inner accretion disc will have reached spin equilibrium (Patterson et al. 2020). Even if our interpretation of the 424.4 s signal is incorrect, this corresponds to a large enough co-rotation radius and a high enough fall-height that the assumption has an insignificant effect on our measurement of the WD mass.

As a further check on our model, we consider an alternative and independent estimate of the shock temperature for IPs. The ratio of Fe XXV and Fe XXVI ionization states depends on the temperature of the emitting plasma, and is therefore an independent measure of the shock temperature of the accretion column (Ezuka & Ishida 1999; Xu, Wang & Li 2016) and can be used to approximate the WD mass (Yu et al. 2018; Xu, Yu & Li 2019). We calculate that ratio by dividing the measured normalizations of the Gaussian lines at 6.97 and 6.70 keV to be 0.57 ± 0.27 , and this ratio is consistent for both the bremsstrahlung continuum model and our PSR model. Following Xu et al. (2019), this would suggest a maximum plasma temperature in the range of 10–40 keV, which falls just below the lower limit of our MKCFLOW model temperature at 47 keV. While estimating the WD mass using the Fe line ratio is not particularly precise, it provides an entirely independent check on the value taken from continuum methods like the PSR model.

In recent years, *NuSTAR* observations have been effective constraining the masses of a number of mCVs, due to the high-energy coverage and sensitivity of the instrument (Hailey et al. 2016; Suleimanov et al. 2016, 2019; Shaw et al. 2018, 2020). Our measured mass of $1.06_{-0.10}^{+0.19} M_{\odot}$ for IGR J18007 is on the higher side of the mass distribution for mCVs, which have an average mass of $\sim 0.8 M_{\odot}$ (Shaw et al. 2020). Still, we trust our WD mass measurement to be robust, considering that we measure a relatively high bremsstrahlung temperature (only two of the sources in Shaw et al. 2020 have a higher temperature), and considering that similar and higher mass IPs are common (e.g. Tomsick et al. 2016; de Martino et al. 2020).

Furthermore, our models provide an excellent statistical fit to the broad spectrum of IGR J18007 from 0.3–79 keV rather than relying on only the high-energy spectrum as some studies have (Suleimanov et al. 2018; Shaw et al. 2020).

Although IGR J18007 is not near the Chandrasekhar limit, it is still above the average mass of WDs in mCVs, and demonstrates that follow-up studies of CVs discovered by *INTEGRAL* will likely have high masses (as another example, see Tomsick et al. 2016). Understanding the mass distribution of accreting magnetic WDs, especially when compared with the average mass of isolated and non-magnetic WDs ($\sim 0.5 M_{\odot}$), is crucial in explaining the formation and evolution of mCVs (Zorotovic, Schreiber & Gänsicke 2011; Shaw et al. 2020). For example, continuing to discover massive accreting WDs will provide insight into whether or not accretion and subsequent novae will raise or lower a WD’s mass over time. Finally, while CVs are worthy of study on their own, the prospect of accreting WDs as progenitors to Type Ia supernovae is of great interest to astrophysics more broadly, and compels us to continue to identify and study sources on the high end of the CV mass distribution.

5 CONCLUSIONS

We confirm the suggested identity of IGR J18007 as that of an IP based on our analysis of simultaneous *XMM* and *NuSTAR* observations alongside optical/IR counterpart photometry. We detect two significant periodic signals in the *XMM* data, the stronger of which occurs at 424.4 ± 0.7 s. This signal has a soft spectrum, and we interpret it as the WD spin period. We also measure the WD mass to be $1.06_{-0.10}^{+0.19} M_{\odot}$ based on our spectral modelling. We also find that a soft component is required in order to satisfactorily fit the spectrum, which we model with a single-temperature blackbody of 73_{-6}^{+8} eV. This paper adds IGR J18007 to the population of well-studied IPs, and further follow-up of similar hard X-ray Galactic sources detected with *INTEGRAL* will continue to improve our understanding of these sources.

ACKNOWLEDGEMENTS

BMC acknowledges partial support from the National Aeronautics and Space Administration (NASA) through Chandra Award Numbers GO7-18030X and GO8-19030X issued by the Chandra X-ray Observatory Center, which is operated by the Smithsonian Astrophysical Observatory under NASA contract NAS8-03060. JAT acknowledges partial support from NASA under NuSTAR Guest Observer grant 80NSSC21K0064. MC acknowledges financial support from the Centre National d’Etudes Spatiales (CNES). JH acknowledges support from an appointment to the NASA Postdoctoral Program at the Goddard Space Flight Center, administered by the Universities Space Research Association under contract with NASA. RK acknowledges support from the Russian Science Foundation (grant 19-12-00369). This work used data from the NuSTAR mission, a project led by the California Institute of Technology, managed by the Jet Propulsion Laboratory, and funded by the National Aeronautics and Space Administration. This research has used the NuSTAR Data Analysis Software (NuSTARDAS) jointly developed by the ASI Science Data Center (ASDC, Italy) and the California Institute of Technology (USA).

DATA AVAILABILITY

Data used in this paper are available through NASA’s HEASARC and the *XMM–Newton* Science Archive (XSA).

REFERENCES

- Anders F. et al., 2019, *A&A*, 628, A94
 Arnaud K. A., 1996, in Jacoby G. H., Barnes J., eds, in ASP Conf. Ser. Vol. 101, *Astronomical Data Analysis Software and Systems V*. Astron. Soc. Pac., San Francisco, p. 17
 Bailer-Jones C. A. L., Rybizki J., Foesneau M., Demleitner M., Andrae R., 2021, *AJ*, 161, 147
 Beuermann K., Burwitz V., Reinsch K., 2012, *A&A*, 543, A41
 Bird A. J. et al., 2016, *ApJS*, 223, 15
 Buccheri R. et al., 1983, *A&A*, 128, 245
 de Martino D., Bernardini F., Mukai K., Falanga M., Masetti N., 2020, *Adv. Space Res.*, 66, 1209
 Ezuka H., Ishida M., 1999, *ApJS*, 120, 277
 Gaia Collaboration, 2021, *A&A*, 649, A1
 Hailey C. J. et al., 2016, *ApJ*, 826, 160
 Harrison F. A. et al., 2013, *ApJ*, 770, 103
 Jansen F. et al., 2001, *A&A*, 365, L1
 Krivonos R. A., Tsygankov S. S., Mereminskiy I. A., Lutovinov A. A., Sazonov S. Y., Sunyaev R. A., 2017, *MNRAS*, 470, 512
 Krivonos R., Sazonov S., Kuznetsova E., Lutovinov A., Mereminskiy I., Tsygankov S., 2022, *MNRAS*, 510, 4796
 Magdziarz P., Zdziarski A. A., 1995, *MNRAS*, 273, 837
 Mukai K., 2017, *PASP*, 129, 062001
 Mushotzky R. F., Szymkowiak A. E., 1988, in Fabian A. C., ed., *NATO Advanced Study Institute (ASI) Series C Vol. 229, Cooling Flows in Clusters and Galaxies*. Kluwer Academic Publishers, Dordrecht, Boston and London, p.53
 Nauenberg M., 1972, *ApJ*, 175, 417
 Norton A. J., Watson M. G., 1989, *MNRAS*, 237, 853
 Patterson J. et al., 2020, *ApJ*, 897, 70
 Patterson J., 1994, *PASP*, 106, 209
 Shaw A. W. et al., 2020, *MNRAS*, 498, 3457
 Shaw A. W., Heinke C. O., Mukai K., Sivakoff G. R., Tomsick J. A., Rana V., 2018, *MNRAS*, 476, 554
 Strüder L. et al., 2001, *A&A*, 365, L18
 Suleimanov V., Revnivtsev M., Ritter H., 2005, *A&A*, 435, 191
 Suleimanov V., Doroshenko V., Ducci L., Zhukov G. V., Werner K., 2016, *A&A*, 591, A35
 Suleimanov V. F., Poutanen J., Werner K., 2018, *A&A*, 619, A114
 Suleimanov V. F., Doroshenko V., Werner K., 2019, *MNRAS*, 482, 3622
 Tomsick J. A. et al., 2020, *ApJ*, 889, 53
 Tomsick J. A., Krivonos R., Wang Q., Bodaghee A., Chaty S., Rahoui F., Rodriguez J., Fornasini F. M., 2016, *ApJ*, 816, 38
 Turner M. J. L. et al., 2001, *A&A*, 365, L27
 Warner B., 2003, *Cataclysmic Variable Stars*. Cambridge University Press, Cambridge, UK
 Wilms J., Reynolds C. S., Begelman M. C., Reeves J., Molendi S., Staubert R., Kendziorra E., 2001, *MNRAS*, 328, L27
 Xu X.-j., Wang Q. D., Li X.-D., 2016, *ApJ*, 818, 136
 Xu X.-j., Yu Z.-l., Li X.-d., 2019, *ApJ*, 878, 53
 Yu Z.-L., Xu X.-J., Li X.-D., Bao T., Li Y.-X., Xing Y.-C., Shen Y.-F., 2018, *ApJ*, 853, 182
 Zorotovic M., Schreiber M. R., Gänsicke B. T., 2011, *A&A*, 536, A42

This paper has been typeset from a $\text{\TeX}/\text{\LaTeX}$ file prepared by the author.